In silico repurposed drugs against monkeypox virus

Hilbert LAM Yuen In [A, B], GUAN Jia Sheng [A], MU Yuguang [A]
(CORRESPONDING AUTHOR)
[A] - School of Biological Sciences, Nanyang Technological University, Singapore, 60 Nanyang Dr, Singapore 637551
[B] - A*STAR Skin Research Labs, Agency of Science, Technology and Research, Singapore, 11 Mandalay Rd, #17-01, Singapore 308232
Keywords: monkeypox, drug repurposing, epidemic, poxviruses, *in silico*

Abstract

Monkeypox is an emerging epidemic of concern. The disease is caused by the monkeypox virus and an increasing global incidence with a 2022 outbreak that has spread to Europe amid the COVID-19 pandemic. The new outbreak is associated with novel, previously undiscovered mutations and variants. Currently the US Food and Drug Administration (FDA) approved poxvirus treatment involves use of tecovirimat. However, there is limited pharmacopoeia otherwise, and limited research interest in monkeypox. In this study, virtual screening and molecular dynamics were employed to explore the potential repurposing of multiple drugs previously approved by the FDA or other jurisdictions for other applications. Several drugs are predicted to tightly bind to viral proteins which are crucial in viral replication, including molecules which show high potential for binding the monkeypox D13L capsid protein, whose inhibition has previously been demonstrated to suppress viral replication.

Introduction

The monkeypox virus belongs to the clade *Orthopoxviruses*, which groups with smallpox, cowpox, vaccinia, and variola [1], and is endemic to West and Central Africa.

Previously, infections have been reported mainly in Central Africa, with the first case being diagnosed in the Democratic Republic of Congo (DRC) in 1970 [2]. A review by Bunge *et al.*, 2022 indicated varying fatality rates ranging from 3.6% to 10.6% between different strains of monkeypox across Africa [2], hypothesising a growing potential for lethality. As of late, monkeypox cases have been found exported into Singapore [3], the United Kingdom [4], Israel [5] and the United States [6] by travellers. An outbreak in the United States Midwest in 2003 was linked to prairie dog contact from infected rodents from Ghana [7]. None of these outbreaks had reported deaths due to monkeypox, however, the reported cases of these outbreaks ranged from a single case in Singapore, United Kingdom and Israel, to 71 cases in the United States in the 2003 outbreak.

Transmission of monkeypox occurs by animal bite or direct contact with an animal's bodily fluids [7]. It can also spread through respiratory droplets during direct and/or prolonged face-to-face contact, through direct contact with bodily fluids of an infected person, or via viral particle contaminated objects [7]. In the current outbreak, monkeypox is being debated as a sexually transmitted disease (STD) [8]. Prevention of monkeypox is 85% effective with the smallpox

vaccine [9].

Monkeypox symptoms present as fever ranging between 38.5°C to 40.5°C, malaise, rash, and headaches. Most tellingly, hard and deep, well-circumscribed and umbilicated lesions are present with swelling of lymph nodes [1].The monkeypox incubation period ranges from 7 - 17 days, with fever declining after three days of rash onset [1]. The lesions are noted to be swollen, stiff and painful. Lymphadenopathy, which presents in monkeypox but not smallpox, have been hypothesised to elicit a stronger immune response as compared to smallpox [10]. Following the lesional segment, scabs are formed and eventually shed off, leading to discoloured spots [5]. Instances of sepsis due to lesions have been reported but are generally accepted to be rare [11].

Monkeypox is diagnosed through PCR, culture, immunohistochemistry such as ELISA, or electron microscopy, depending on test availability [5, 9]. Viral particles from the case investigated by Erez *et al*., 2019, showed a particle size of 281 ± 18 nm × 220 ± 17 nm (n = 24). Treatment of monkeypox is supportive [9].

Currently identified potential treatments include tecovirimat, which is approved by the US FDA for the treatment of smallpox. Cidofovir or brincidofovir have also been listed as possibly effective for monkeypox treatment, however their use has not been studied outside of experimental models [9]. Application of other drugs have not been widely explored and therefore an open knowledge gap exists in monkeypox treatment.

The monkeypox genome is similar to that of smallpox, with a previous study showing 96.3% identity in the central regions, which encodes essential enzymes and proteins [12]. Monkeypox genome nomenclature follows that of universal nomenclature, however differing at certain regions which encode for virulence [13]. Out of all Poxviridae, vaccinia is one of the most well studied due to its use in vaccination against other types of poxviruses [14] and being a much less dangerous relative of smallpox [15]. Monkeypox, smallpox and vaccinia have a genome size of approximately 197 kb [16], 186 kb [17] and 190 kb respectively [18]. All poxvirus genomes are linear, double-stranded DNA.

For clarity in this work, due to the similarities and naming difficulties of other poxvirus homologues, the authors will refer to the targets, homologues or otherwise, after vaccinia nomenclature as the universal nomenclature gene name as in vaccinia virus. Five poxvirus targets are investigated: (a) A48R, (b) A50R, (c) D13L protein trimer complex, (d) F13L, and (e) I7L, all of which have been proposed as useful intervention targets by other studies and reviews [19]. A50R, D13L, F13L and I7L were chosen due to previous literature supporting *in vitro* or *in vivo* evidence for their efficacy, whereas A48R has been previously identified to be a good potential drug target [19].

(a) A48R is a thymidylate kinase previously determined to complex with thymidine diphosphate [20] and is a novel target in the sense that it is currently not targeted by any known drugs. The

function of A48R is to phosphorylate thymidine monophosphate to its diphosphate, and also to phosphorylate 5′ halogenated deoxyuridine monophosphate analogues [19]. The substantial structural difference from human thymidylate kinase at the active site [20] makes it an attractive target for other thymidine analogues without excessive concern of interfering with the human analogue's function.

(b) A50R is a DNA ligase known to be inhibited by mitoxantrone. N-terminal mutations of this protein demonstrated instances of antiviral resistance. The resistance mutations location pinpointing its active site towards this location [21] and make it a valuable target for drug discovery. Mitoxantrone has also been shown to be unique amongst inhibitors identified, in that it has no impact on viral gene replication [21] but clear microscopic evidence shows that it blocks assembly of viral particles by an unknown mechanism [21].

(c) D13L is a protein trimer complex and major capsid protein which lends rigidity to the membrane and is especially important in viral particle morphogenesis [22]. In previous studies, rifampin has been demonstrated to have an affinity for the D13L protein in vaccinia virus [19]. Rifampin, synonym rifampicin, is an antibiotic produced by the soil bacteria *Amycolatopsis rifamycinica*, and is used to treat tuberculosis, leprosy, and MRSA [23]. It has separately been demonstrated to inhibit poxvirus assembly by binding to the D13L trimer complex, a mechanism independent of its antibacterial activity [24]. Unfortunately, the rifampin effect of halting viral replication is reversible, with assembly reinitiating within minutes after drug withdrawal [25]. Clinically, rifampin is not used due to emergence of mutant, rifampin-resistant viruses [26], but with a larger pharmacopoeia, the authors propose that this problem may be overcome using drug cocktails. Despite the current lack of clinical use of rifampin in treating poxvirus infections, the D13L docking site was derived from X-ray crystallography in complex with rifampin [24], providing a targetable active docking site for drug design. In previous studies, rifampin has exhibited *in vitro* depression of vaccinia-directed protein synthesis and cowpox viral particles in HeLa-S_2 cells [27]. The anti-poxviral activity of rifampin and how the lengthening or shortening of chains have also previously been explored and found to affect specific antiviral activity [28]

(d) F13L is the current target of the only approved drug for poxvirus treatment, tecovirimat (previously known as ST-246). It is a major envelope protein and is also a palmitoylated membrane protein [19], making it vital for the extracellular envelope virus (EEV) formation and important for viral entry into the cell [29]. Tecovirimat has been shown to be strongly efficacious in animal models [30].

(e) I7L core proteinase is a cysteine proteinase which cleaves the major structural and membrane proteins of viruses [31]. Proteases are ideal therapeutic targets due to their essential function in viral replication by cleaving precursor polyproteins [32], and protease inhibitors in other viruses such as HIV have shown promise for other viral protease inhibitors [33]. As such, monkeypox virus proteases are also attractive targets to inhibit viral replication. Previous studies identified TTP-6171 as an inhibitor of I7L. However, drug resistant I7L could also be generated with mutations [31].

After deriving these targets, the authors identified the active protein residues in monkeypox using multiple sequence alignments and consequently propose eight novel potentially repurposable drugs. These eight drugs are: NMCT and rutaecarpine for A48R, nilotinib for A50R, simeprevir for D13L, hypericin and naldemedine for F13L, and fosdagrocorat and lixivaptan for I7L.

Method

Multiple sequence alignment with other poxviruses. Poxvirus sequences were obtained from NCBI Nucleotide database (GenBank and EMBL accessions: ON585029.1 - monkeypox, Portuguese 2022 isolate, ON568298.1 - monkeypox, 2022 German isolate, ON602722.1 - monkeypox, 2022 French isolate and LT706528.1 - smallpox, historical sample). Proteins of interest were identified using tBLASTn 2.12.0+, translated using the ExPASY [34] translate tool and subsequently aligned using MultAlin [35].

Structures used for virtual screening and Molecular dynamics (MD). A48R and D13L structures were modelled using previously experimentally determined structures, PDB 2V54 and 6BED respectively. Additional hydrogen atoms were not augmented onto the experimentally determined proteins. A50R, F13L and I7L were modelled using AlphaFold2 [36] with a ColabFold wrapper [37]. The protein sequences used were from the German isolate of monkeypox, extracted using tBLASTn 2.12.0+ (NCBI accessions - A50R: AAO89455.1, F13L: AAO89331.1, I7L: AAO89355.1). The extracted sequences were translated using the ExPASY [34] translate tool before AlphaFold2 structural prediction.

Docking site identification from structures. The active sites for A48R and D13L were identified from the location of thymidine and rifampin in their respective PDB structures. A50R, F13L, and I7L active sites were identified from mutation studies in literature [21, 31, 38], and mapped to the monkeypox analogues after multiple sequence alignment.

Reverse docking for pocket validation for AlphaFold2 predicted proteins. Reverse docking was performed using mitoxantrone for A50R, tecovirimat for F13L and TTP6171 for I7L and visual screening performed to validate the correct site.

Molecular screening and docking. QuickVina 2.1 (QVina2.1) [39] was used in conjunction with the ZINC library [40] of FDA drugs and drugs approved by other major jurisdictions (non-FDA), and also DrugBank [41, 42]. Partial charges of ligand molecules were calculated using ADFR Tools [43] using the default Gasteiger charges. Sorting of the top candidates was performed with the top performer having the largest binding affinity score to the site of interest. Manual inspection of docking sites and docking poses were then performed using PyMOL 2.5.0 [44]. PDBQT files from QVina2.1 were converted back into PDB and appended for CHARMM-GUI using OpenBabel 3.1.0 [45]. Docking was performed using mitoxantrone for A50R, tecovirimat for F13L and TTP6171 for I7L and visual inspection was performed to validate the correct binding site.

Molecular dynamics simulations. MD simulations and energy minimisation were performed using GROMACS version 5.1.8 [46]. The CHARMM36m force field was used and added using CHARMM-GUI's solution builder [47, 48] after a separate ligand force field was constructed. GalaxyFill [49] was used as per CHARMM-GUI to fill in gaps present in the X-ray structure of A48R and D13L so that MD could be performed. A cubic periodic boundary condition (PBC) of 1 nm at the farthest end of each protein boundary was established. The protein was solvated in a TIP3P water solvent at 0.15 M of KCl, and energy minimisation performed using the steepest integrator at 0.1 fs for 10,000 iterations, using potential of mean force (PME) for coulomb, non-bonded minimisation. Following which, equilibration was performed at 1 fs for 125,000 iterations, using the verlet integrator, equilibrating the system to 303.15 K. Lastly, a total NPT ensemble simulation of 100 ns was performed at 2 fs per iteration. V-rescale and Parrinello-Rahman were used for temperature (303.15 K) and pressure coupling respectively (1 bar). Position restraints were not used in both steps. Covalent hydrogen bonds were constrained in the equilibration and MD steps.

Assessment of protein stability. Ramachandran plots were used to assess the stability of both AlphaFold2-predicted and experimentally derived protein structures, and were plotted using the Ramachandran plot server [50]. Furthermore, root mean square fluctuation (RMSF) and root mean square distance (RMSD) were calculated to assess stability.

Calculation of MD metrics. RMSD was calculated of the ligand to its initial structure. Minimum distance between the ligand and the receptor and hydrogen bonds were also computed. Hydrogen bonds interactions between each ligand-receptor were also captured with a cutoff radius of 0.35 nm and cutoff angle of 30 degrees. All metrics are calculated at a timestep of 1 ps and performed using GROMACS. Both RMSD and minimum distance were computed after rotation and fitting to the initial structure. RMSF and RMSD of proteins are calculated relative to the initial structure of the protein for all MDs with ligands after centering, adjusting for PBC, and fitting to the pocket of interest.

Clustering and ligand-receptor interaction classification. Clustering was performed using the GROMOS method [51] with a RMSD threshold of 0.3 nm per cluster on a simplified trajectory at 2.5 ns per frame. Ligand plots and associated interactions were determined using LIGPLOT+ (version 2.2.5, 27 January 2022) [52] for the cluster with the highest number of frames.

Results

Protein similarity of monkeypox isolates and chosen docking proteins. High protein similarity was observed throughout poxvirus targets in general (Fig. 1). However, the French isolate showed premature stop codons inserted in all proteins. However, none of the active residues previously identified in literature were mutated (Fig. 1). Lower sequence conservation for I7L was observed near active site residue His-241 due to unclear sequencing of the Portugal isolate. Explorations of the deletions in the French isolate are away from any docking and active sites (Supplementary Fig. 1).

Stability of proteins. Proteins have been shown to be stable (Supplementary Fig. 2), with little unexpected psi and phi angles throughout. Furthermore, the RMSD of the proteins to the initial structure is low (Supplementary Fig. 3), indicating that significant overall conformational changes throughout the simulation was absent. At a local level, the RMSF of residues remained low (mainly below 2 nm) throughout the entire simulation (Supplementary File 2), showing no drastic local changes in conformational structure that could affect docking stability.

Active sites and protein conformation. Sites of deletion are also facing away from the active site (Supplementary Fig. 1) for all isolates tested, indicating limited impact on experimentation.

Table 1: potential drugs derived for monkeypox targets

Gene	Protein function	Reference protein	*In vitro* proven drug	Novel repurposable drug	Drug structure
A48R	Thymidylate kinase	PDB: 2V54 [20]	-	NMCT	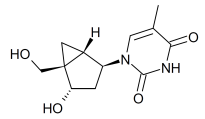
				Rutaecarpine	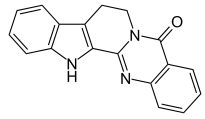
A50R	DNA ligase [19]	AlphaFold2 structure of German monkeypox viral protein identified via tBLASTn	Mitoxantrone [19, 21]	Nilotinib	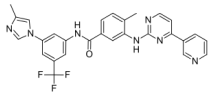

D13L	Viral capsid protein [19]	PDB: 6BED [24]	Rifampin [19]	Simeprevir	
F13L	EEV formation protein [19]	AlphaFold2 structure of German monkeypox viral protein identified via tBLASTn	Tecovirimat [19]	Hypericin	
				Naldemedine	
I7L	Protease [19]	AlphaFold2 structure of German monkeypox viral protein identified via tBLASTn	TTP6171 [19]	Fosdagrocorat	
				Lixivaptan	

Repurposable drugs for A48R. NMCT and rutaecarpine were the drugs chosen (Table 1). The QVina2.1 binding affinity for NMCT and rutaecarpine are -7.0 kcal/mol and -9.0 kcal/mol respectively. Thymidine diphosphate, the native ligand to A48R, has a docking energy of -7.4 kcal/mol. NMCT was chosen due to its previously demonstrated activity in thymidine kinase of poxviruses [53] and the good pose into A48R (Fig. 2). The RMSD of both NMCT and rutaecarpine remained low throughout the simulation (Fig. 3), and both NMCT and rutaecarpine showed hydrophobic interactions (Fig. 4). NMCT was also noted to form strong hydrogen bonds with some of the amino acid residues (Fig. 5). Both NMCT and rutaecarpine also clustered into one single stable cluster for the entire simulation (Table 2), further proving the ligand stability in pocket.

Repurposable drugs for A50R. Nilotinib was the drug chosen (Table 1). It had the highest binding affinity of all drugs screened with a QVina2.1 score of -10.8 kcal/mol. The hydrophilic groups were also observed to be spatially close to the hydrophilic regions of the amino acid

(Fig. 2). Furthermore, nilotinib demonstrated low RMSD throughout the MD simulation, with RMSD generally < 0.9 nm for all instances (Fig. 3), with hydrophobic interactions of the main carbon chain and the amino acids noted (Fig. 4). Overall, nilotinib was chosen due to the evidence *in silico* and due to its relatively longer half life (Table 2).

Repurposable drugs for D13L. Simeprevir was the drug chosen (Table 1). It had a high binding energy of -9.2 kcal/mol to the D13L trimer complex, which is higher than the score of rifampin, the model drug (Fig. 2). Simeprevir is previously used as an antiviral (Table 2) by inhibiting protein synthesis and therefore viral maturation and replication. Hydrogen bonds were noted with existing hydrogen bonds formed by the X-ray derived rifampin (Fig. 5). RMSD also showed less fluctuation compared to rifampin (Fig. 3), showing strong binding stability and its potential to be a more potent inhibitor of D13L.

Repurposable drugs for F13L. Hypericin and naldemedine are the chosen drugs for F13L (Table 1), with the binding affinity of -11.2 kcal/mol and -10.1 kcal/mol respectively, both of which higher than the control drug tecovirimat of -8.4 kcal/mol (Fig. 2). Hypericin showed a particularly interesting pose. Being a honeycomb-like shape it fits snugly into the F13L pocket, with the hydrophilic ends interacting accordingly with the protein (Fig. 2). Two hydrogen bonds were also noted between hypericin and the neighbouring amino acid residues (Fig. 4). Naldemedine was also noted to have a combination of both hydrophobic and hydrophilic areas, with the hydrophilic nitrogen group binding appropriately. In simulation, both drugs showed consistent RMSD values of < 0.5 nm (Fig. 3), and clusters of the most stable conformations make up > 95% of the entire simulation length, further highlighting the stability of hypericin and naldemedine in simulation (Table 2). Multiple non-transient hydrogen bonds were also observed for naldemedine (Fig. 5), further emphasising the *in silico* stability of the structure. Naldemedine also showed many hydrophobic interactions with the neighbouring F13L protein residues (Fig. 4).

Repurposable drugs for I7L. Fosdagrocorat and lixivaptan (Table 1) were both identified to have the strongest binding affinity of drugs screened at -10.1 kcal/mol compared to control TTP6171, at -9.3 kcal/mol. Both fosdagrocorat and lixivaptan showed increased stability to the binding site, with much lower RMSD and low fluctuation of the RMSD throughout simulation (Fig. 2). A strong hydrogen bond was also observed for fosdagrocorat throughout the simulation. The presence of aromatic rings in both fosdagrocorat and lixivaptan also allows for pi-stacking, further increasing factors that stabilise the ligand position in protein (Fig. 2).

Overall docking affinities of all screened drugs. Overall docking showed that ligands fitted generally within 0.3 nm of the active site for all targets, though with varying binding affinities (Fig. 2). Outside of mitoxantrone, all other established drugs had a stronger binding affinity than

the average of the drug library (Fig. 2). All binding energies of docked drugs are available in Supplementary File 1.

Readjustment of poses in simulation. TTP-6171 as a control for I7L was found to have higher RMSD but stabilised more at a later stage of the simulation due to the drug changing to a different extended conformation which still binds near to the active site residues. However, its RMSD every 2.5 ns exceeded the clustering threshold of 0.3 nm, and as a result was not binned into sets > 1 cluster (Table 2).

Hydrophobic interactions in most stable conformation identified through clustering. For A48R, 8 and 9 hydrophobic interactions for NMCT and rutaecarpine were identified. For A50R, 7 were identified for the control mitoxantrone, and 10 for nilotinib. For D13L, 9 for the control rifampin and 5 for simeprevir. 5, 6, and 12 hydrophobic interactions were found for F13L for the drugs tecovirimat (control), hypericin, and naldemedine respectively. Lastly, 7, 6, and 7 hydrophobic interactions were found for I7L for the control drug TTP6171, fosdagrocorat and lixivaptan. The high number of hydrophobic interactions generally corresponded to a lower RMSD value as from the MD simulations.

Table 2: drug binding stability in simulation and pharmacology

Target	**Drug**	**Largest cluster middle RMSD / nm**	**Top cluster proportion / %**	**Drug half-life**	**Current drug uses**
A48R	NMCT	0.172	100.00	3.7 h (in-vitro cells only)	Nucleoside analogue, potent viral inhibitor, not used in humans [54]
	Rutaecarpine	0.173	100.00	Unknown	COX-2 inhibitor for headache, abdominal pain in traditional Chinese medicine [55]
A50R	Mitoxantron	0.217	90.24	75 h [41]	Multiple

	e (control)				sclerosis [41]
	Nilotinib	0.238	29.27	15 h [41]	Leukaemia [41]
D13L	Rifampin / rifampicin (control)	0.175	100.00	3.35 (± 0.66) h [41]	Antibiotic [41]
	Simeprevir	0.193	90.24	10 - 13 h [41]	Antiviral [41]
F13L	Tecovirimat (control)	0.222	100.00	21 h (intravenous), 19 h (oral) [41]	Poxvirus treatment [41]
	Hypericin	0.194	97.56	24.8 - 26.5 h [56]	Supplement, part of St. John's Wort
	Naldemedine	0.219	100.00	11 h [41]	Opioid-induced constipation [41]
I7L	TTP6171 (control)	-	-	Unknown	Protease inhibitor, not used in humans
	Fosdagrocorat	0.214	56.10	Unknown	Rheumatoid arthritis [41]
	Lixivaptan	0.256	58.54	11 h [57]	Hyponatremia, congestive heart failure [41]

Hydrogen bonding for experimentally derived structures. Hydrogen bonds were observed between ligand-receptors throughout the simulation (Figure 5). In A48R, NMCT formed a consistent hydrogen bond with Asp-13 and Arg-72. Rutaecarpine showed transient hydrogen bond formation. In D13L, consistent hydrogen bonding between Gln-27 was observed for both the control rifampin and simeprevir, indicating a potentially active and important site.

Hydrogen bonding for AlphaFold2 derived structures. Many residues overlap in hydrogen bond formation with the ligand in A50R, F13L, and I7L. A50R displayed inconsistent hydrogen bonds throughout the simulation for all drugs but strong hydrogen bonding for Lys-157 in mitoxantrone and Arg-8 in nilotinib. F13L showed a potential hotspot residue of Arg-89 and Ser-135, binding all three drugs investigated. Furthermore, for F13L, all drug targets showed formation of hydrogen bonds in their most stable conformations identified through clustering, with hypericin forming two separate hydrogen bonds with structurally neighbouring residues Ser-327 and Asn-329. For I7L, TTP-6171, the control drug, was observed to form hydrogen bonds with the greatest number of residues. However, TTP-6171 and lixivaptan did not form stable hydrogen bonds with any of the residues. Only fosdagrocorat was observed to form stable hydrogen bonds with residue Asp-258 and Gly-261, with two hydrogen bonds to each residue in total for its most stable conformation (Fig. 4).

Table 3: active residues in identified targets and potentially new active residues of interest

Gene	**Active residues (per literature) *relative to* reference protein**	**Potentially new active residues of interest (per results) *relative* to reference protein**
A48R	Asn-65, Leu-111, Lys-105, Ala-107 (structural study) [20]	Tyr-144
A50R	Cys-11, Cys-147 (mutation study) [21]	Lys-9, Tyr-15, Asn-143, Asn-146
D13L	Phe-168, Phe-486, Phe-487 (mutation study) [58]	-
F13L	Gly-277, Asp-280 (mutation study) [38]	Ser-135, Asp-280,, Asn-329, Asp-331
I7L	His-241, Cys-328 (mutation study) [31]	Ser-240, Lys-243

Overall consistency of non-bonded interactions to previously elucidated active residues in literature. For A48R, hydrogen bonding was observed for both NMCT and rutaecarpine to Asn-65 and Lys-105 throughout the simulation. In addition, an additional amino acid of interest, Tyr-144 (Table 3), was identified, as both NMCT and rutaecarpine showed affinity for it throughout the simulation in the form of hydrogen bonds (Fig. 5). No hydrophobic interactions in the most consistent cluster are consistent with the ones previously identified in literature. For A50R, Cys-11 showed hydrophobic interactions with the ligands identified. Hydrogen bonding was also observed for mitoxantrone at Cys-11, but not for nilotinib. However, strong hydrogen bonding was observed in neighbouring amino acids, namely Lys-9, Tyr-15, Asn-143, and Asn-146 (Table 3). Hydrophobic interactions in D13L are consistent with the literature of the Phe-486 active site for the control drug rifampin; simeprevir also showed hydrophobic interactions with these residues. Moreover, these interactions are also found in the native X-ray structure, before simulation (Supplementary Fig. 4). F13L showed a very high number of hydrogen bonding in general (Fig. 5), with tecovirimat, the control drug, forming hydrogen bonds with Asp-280 (Table 3). However, hypericin and naldemedine did not form hydrogen bonds throughout the 100 ns simulation with Asp-280. New residues of interest, Ser-135, Asn-329, Asp-331 and especially Asn-312 were identified from the hydrogen bonding (Table 3). Asn-312 was observed to form hydrogen bonding with all the drugs tested, including tecovirimat. Moreover, in the most stable conformation, Asn-312 formed hydrophobic interactions with both hypericin and naldemedine. The results clearly show the hydrogen bonds being pivotal to stabilising the structure, as these structures merely vibrated in place in simulation (with the exception of tecovirimat, which flipped). Lastly, for I7L, Hydrogen bonds were also noted at His-241 and neighbouring residues Ser-240 and Lys-243. His-241 also showed hydrophobic interactions with fosdagrocorat and lixivaptan (Table 3).

Screening of other molecules in addition to those listed. In addition to molecules listed, molecular screening and MD were also performed on the AlphaFold2-derived structure of protease G1L. Molecules screened for these targets dislodged during the MD. Other drugs that dislodged during the MD, or otherwise showed unstable conformations are: cinacalcet for A48R, ponatinib and vitamin D for A50R, rifaximin, glecaprevir and dutasteride for D13L, lifitegrast for F13L, baloxavir, laniquidar, nilotinib, DB06925, DB04727 and DB11913 for I7L, TMC-647055, cepharanthine, fda_1667 and fda_1348 for G1L. These drugs showed RMSD values of > 1 consistently throughout the simulation, with all the drugs tested dislodging from the pocket of interest, and therefore determined to be of limited binding capability to G1L. All binding energies, drug SMILES, and other IDs of these screened drugs can be found in Supplementary File 1.

Discussion

Amino acid polymorphisms. Overall, a large number of polymorphisms, premature stop codons and duplications were observed in the French isolate for all proteins investigated. The positions of these polymorphisms are not on any key active residues and are generally conserved, despite the broken frames. There is no reported additional virulence on the French isolate as to date, and given the low possibility of large number of protein deletions and mutations relative to other isolates gathered during the same time, the sequencing depth may be insufficient, and further sequencing and exploration of this isolate is required.

Potential of screened drugs *in silico*. All drugs tested showed high stability in MD simulations with the CHARMM36m force field (Fig. 3). This is further validated by hydrophobic contacts (Fig. 4), indicating higher potential as a monkeypox treatment option. The results also demonstrate that the number of hydrophobic contacts are potential contributing factors to the drug stability.

***In silico* confirmation of A50R, F13L and I7L binding sites.** Stability and clustered poses (Fig. 3, Supplementary Fig. 5) confirm structural active and binding sites for AlphaFold2 derived proteins. Mitoxantrone and tecovirimat have been shown to dock strongly and stably to the pockets near the active sites in the entire simulation. This is *in silico* evidence for the location of the pocket, and further validation of previous work that proved the efficacy of said drugs in inhibiting poxviruses [19]. TTP-6171 also showed relatively good binding to the I7L pocket, further proving its ability to stop viral replication [31] and further making its case of being a potential drug to treat monkeypox.

Elucidation of potentially new residues of interest. For A48R, a new amino acid of interest, Tyr-144 was identified. Gln-27 for D13L also showed hydrogen bonding to both rifampin and simeprevir, highlighting its potential importance for future studies. Ser-135, Asn-329, Asp-331 and Asn-312 are the other residues noted of importance for F13L (Fig. 4-5). The importance of these residues may further facilitate the drug discovery process for other poxviruses, and as a watch point for potential antiviral resistance mutations.

Half-life, contraindications, side effects and bioavailability of drugs. NMCT (for target A48R) is a potent antiviral that has not been used clinically and is not currently approved, but has potential potent antiviral activity in HSV-2-infected mice [59], with little apparent cytotoxicity in uninfected Vero cells [60]. In addition to being demonstrated in this study *in silico* for being effective in blocking A48R, NMCT also has known effects in halting viral replication by targeting J2R, a thymidine kinase in vaccinia [53]. This property of NMCT makes it a possible double-action drug in the fight against monkeypox.

Rutaecarpine (for target A48R) is a COX-2 inhibitor and is touted as an anti-inflammatory [61]. It is isolated in a traditional Chinese medicine “Wu-Chu-Yu” (吴茱萸) and has been officially incorporated into the Chinese Pharmacopoeia 2015 Edition [55]. It is, however, not approved by the FDA and the half-life is unknown. The fruit that it is found in also contains other alkaloids as part of the Rutaceae family.

Nilotinib (for target A50R) is an orally administered, FDA approved drug for the treatment for chronic myelogenous leukaemia (CML). It has an adverse drug effect in patients with a polymorphism in UGT1A1. Otherwise, it has demonstrated safety in human trials [41].

Simeprevir (for target D13L) binds extensively to plasma proteins, mainly albumin [41]. Simeprevir has previous use in treating HCV and its high oral bioavailability of 44% makes it a potentially good target [62]. It is also to be noted that use of simeprevir is contraindicated in those with asymptomatic hepatitis B virus (HBV) infection, as usage can lead to reactivation of the virus and subsequent symptomatic disease [63].

Hypericin (for target F13L) is a naturally occurring substance found in St. John’s Wort that can also be separately synthesised [64]. It can induce photo-cytotoxicity [65] and has been touted as a potential treatment and detection of cancer [64]. The photosensitising effects of hypericin has also shown efficacy of it being a multimodal antiviral [66], and has been long-known to inactivate murine cytomegalovirus (MCCV) and HIV-1, especially with exposure to fluorescent light [67]. However, the use of St. John’s Wort, by extension hypericin, in combination with other medicines, has previously proven an antagonistic effect [68] and could interfere with contraceptives [69]. Otherwise, it is well tolerated [70].

Naldemedine (for target F13L) is a peripherally acting μ-opioid receptor antagonist for opioid-induced diarrhoea in adults with chronic pain [71]. It is generally well-tolerated, even in the long-term, and does not cause opioid withdrawal [72]. A previous phase III trial has demonstrated it to be safe and effective [73]. However it has a relatively short half-life of 11 h, and constant administration may be required. Side effects include headache, nausea, and bowel dysfunction [71].

Fosdagrocorat (for target I7L) was reported to not be absorbed systemically post oral administration [74]. Therefore, IV administration may be used as a possible alternative solution for drug uptake.

Lixivaptan (for target I7L) is an orally active, non-peptide, competitive, and selective antagonist for the vasopressin V2 receptor which functions by promoting the excretion of retained body water [75]. Half-life of lixivaptan is approximately 11 hours [57]. The longer half-life allows the drug to be present for a longer duration and exhibit its suitability as a potential I7L inhibitor.

Antiviral resistance towards derived drugs. Rifampin, a previously identified drug that binds to D13L has previously not been used as an antiviral in treating poxvirus infections due to development of antiviral resistance [24]. Moreover, the presence of a strong Gly-27 bond between D13L and both simeprevir and rifampin indicate a possible hotspot for antiviral resistance, for a mutation of this molecule may signal a loss of a strong, consistent hydrogen bond. In other sites, previous mutations in vaccinia have also shown resistance to mitoxantrone and tecovirimat [19, 31]. It is through these sites that the active residues were identified, however, these mutations may also equally render other drugs useless. In order for this to be overcome, a drug cocktail may be used, such as one prescribed in highly antimicrobial resistant settings [76], to completely wipe out the virus without giving it mutation potential under evolutionary stress.

Limitations of the study. The authors acknowledge four limiting factors (LF) of this study:

LF1. Bioavailability of some drugs is not fully known. Since all targets investigated are found in the cytoplasm of an infected cell, a lack of plasma membrane permeability could result in reduced efficacy. This would make drug titration difficult. Furthermore, some drugs may be metabolised differently *in vivo*, rendering the metabolite not effective.

LF2. Docking and simulations are purely theoretical tools. Due to the imperfectness of the energy functions used, false positive cases cannot be avoided.

LF3. The prediction of structures A50R, F13L, and I7L were done using AlphaFold2. The accuracy of these predictions as a result cannot be fully validated.

LF4. The true efficacy of the repurposed drug cannot be demonstrated *in silico*. More evidence, especially *in vivo* studies are required to ascertain the drugs' usability for monkeypox treatment before it is widely applied.

Conclusion

With zoonotic diseases being of increasing threat to human survivability - and monkeypox amongst other poxviruses are becoming an emerging threat - it is imperative for a greater exploration of pharmacopoeia to address these diseases. The use of potential targets NMCT and rutaecarpine for A48R, nilotinib for A50R, simeprevir for D13L, hypericin and naldemedine for F13L, fosdagrocorat and lixivaptan for I7L and controls named in this paper should be further investigated so as to reduce fatalities caused by viruses. The authors also hope that the uprise of recent pandemics and epidemics, namely COVID-19 and monkeypox, will garner more much needed attention on diseases, currently neglected or otherwise, and attract much warranted research.

Acknowledgements

The authors thank Professor Thomas Larry Dawson, Jr., for extensively reviewing, checking and editing the manuscript for intellectual and academic rigour.

The authors also thank Ms. Ong Xing Er for her contribution in assisting the search for the D13L target in monkeypox, thoroughly designing the layout of figures, and artistic feedback.

The authors declare no conflict of interests in this work.

Author Contributions

Hilbert Lam Yuen In and Guan Jia Sheng performed *in silico* docking and MD simulations for manuscript writing and figure creation.

Mu Yuguang was involved in project design, substantiatively revising the work, and approving the final version submitted.

Abbreviations

MD - molecular dynamics
HSD/HIS - histidine amino acid
RMSD - root mean square deviation
RMSF - root mean square fluctuation

Data availability statement

All QVina2.1 binding affinities for drugs screened are provided as per Supplementary File 1.

Raw molecular dynamics trajectories will be provided by the authors upon request. Please take note that trajectories are > 50 GB each, with all full files (including rotated, centred trajectories, etc.) > 300 GB per MD. Transfer will be at the expense of the requester.

Summarised molecular dynamics trajectories are provided as per Supplementary Figure 2.

Funding

This work is supported by Singapore MOE Tier 1 grant RG27/21. Thomas Larry Dawson and Hilbert Lam Yuen In were supported by funding from Agency for Science, Technology and Research (A*STAR) and A*STAR BMRC EDB IAF-PP grants (H17/01/a0/004, Skin Research Institute of Singapore, and H18/01a0/016, Asian Skin Microbiome Program).

The computational work for this article was partially performed on resources of the National Supercomputing Centre, Singapore (https://www.nscc.sg).

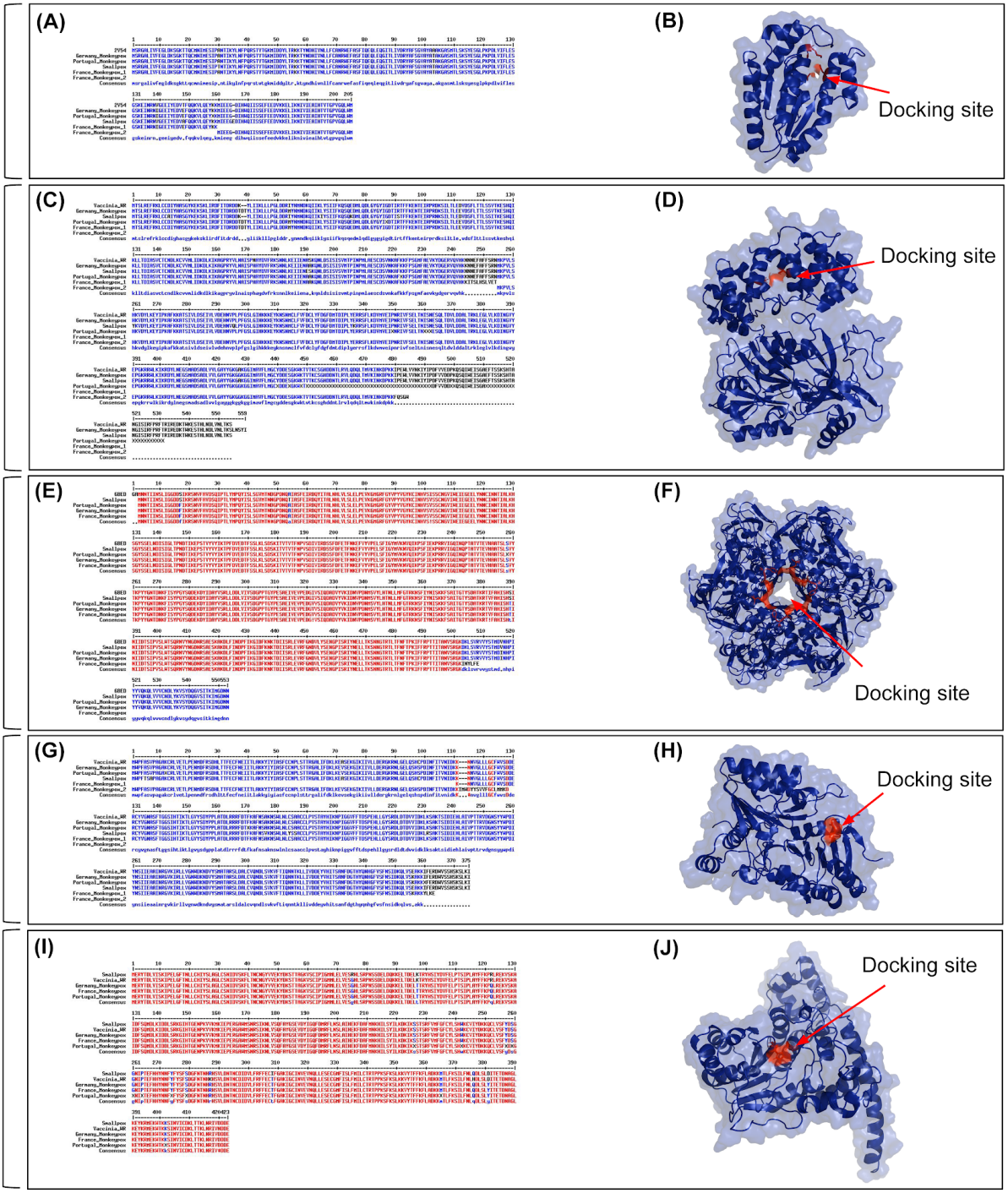

Figure 1. Significant similarity of (a) A48R 2V54, (c) A50R, (e) D13L 6BED, (g) F13L and (i) I7L across vaccinia, smallpox, and monkeypox. Sequences were aligned using MultAlin. Protein structures (b) PDB: 2V54 from vaccinia, (d) AlphaFold2 predicted structure for German isolate A50R protein, (f) PDB: 6BED from vaccinia, (h) AlphaFold2 predicted structure for German isolate F13L protein, and (j) AlphaFold2 predicted structure for German isolate I7L protein.

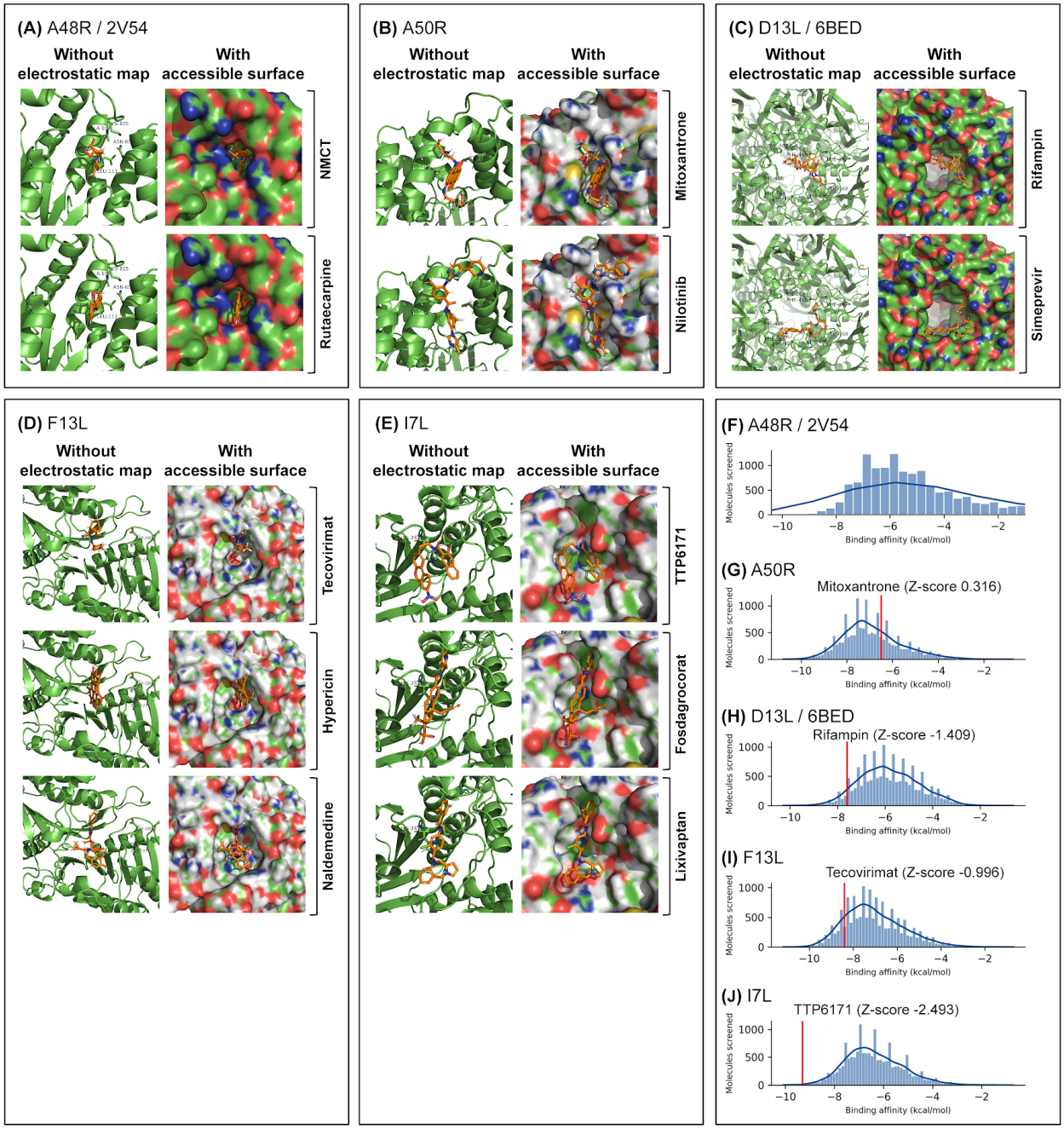

Figure 2: Identified drugs of interest show good fit within docking regions and pockets, and control drugs generally scored higher than the majority of docked drugs, with the exception of mitoxantrone in A50R. Docking was performed using QVina2.1 around the region of interest, with a search box of 30 x 30 angstroms, with the best poses sorted by strongest binding affinity shown. Electrostatic maps with solvent accessible surfaces were calculated using PyMOL, with individual amino acids of importance labelled on diagrams.

Figure 3. High stability of drugs observed in MD simulations, with all novel drugs proposed having an RMSD < 1 and control drugs having an RMSD < 1.3. Molecular dynamics were performed using the CHARMM36m force field. RMSD of ligand was computed to amino acids 1 to 141 for (b) A50R, chain C of 6BED for (c) D13L, and computed to whole protein for the others. Moving averages of 1 ns are plotted respectively.

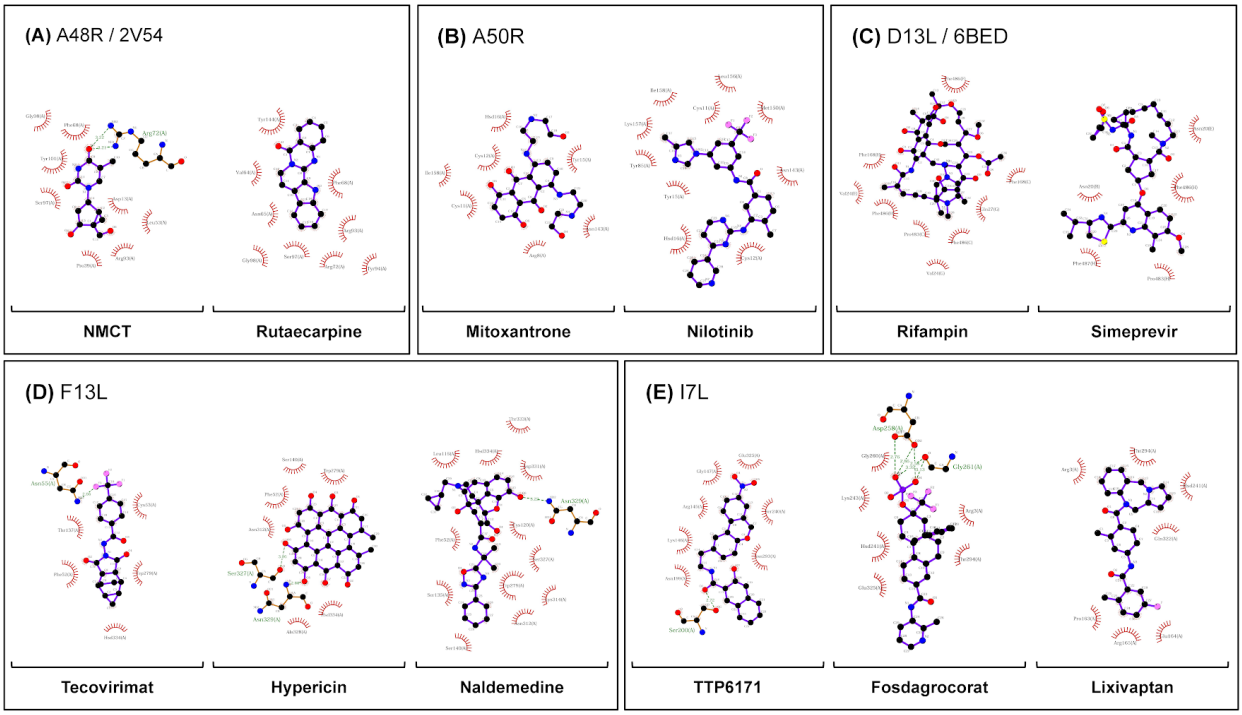

Figure 4: Strong non-bonding interactions observed between most clustered poses of ligands. Structures were clustered using GROMOS force field at a RMSD cutoff of 0.3 nm in GROMACS, with the cluster with highest number of trajectory timesteps analysed. Ions and water molecules were removed before analysis as their interactions are transient. LigPLOT+ was used to generate the ligand interaction figures.

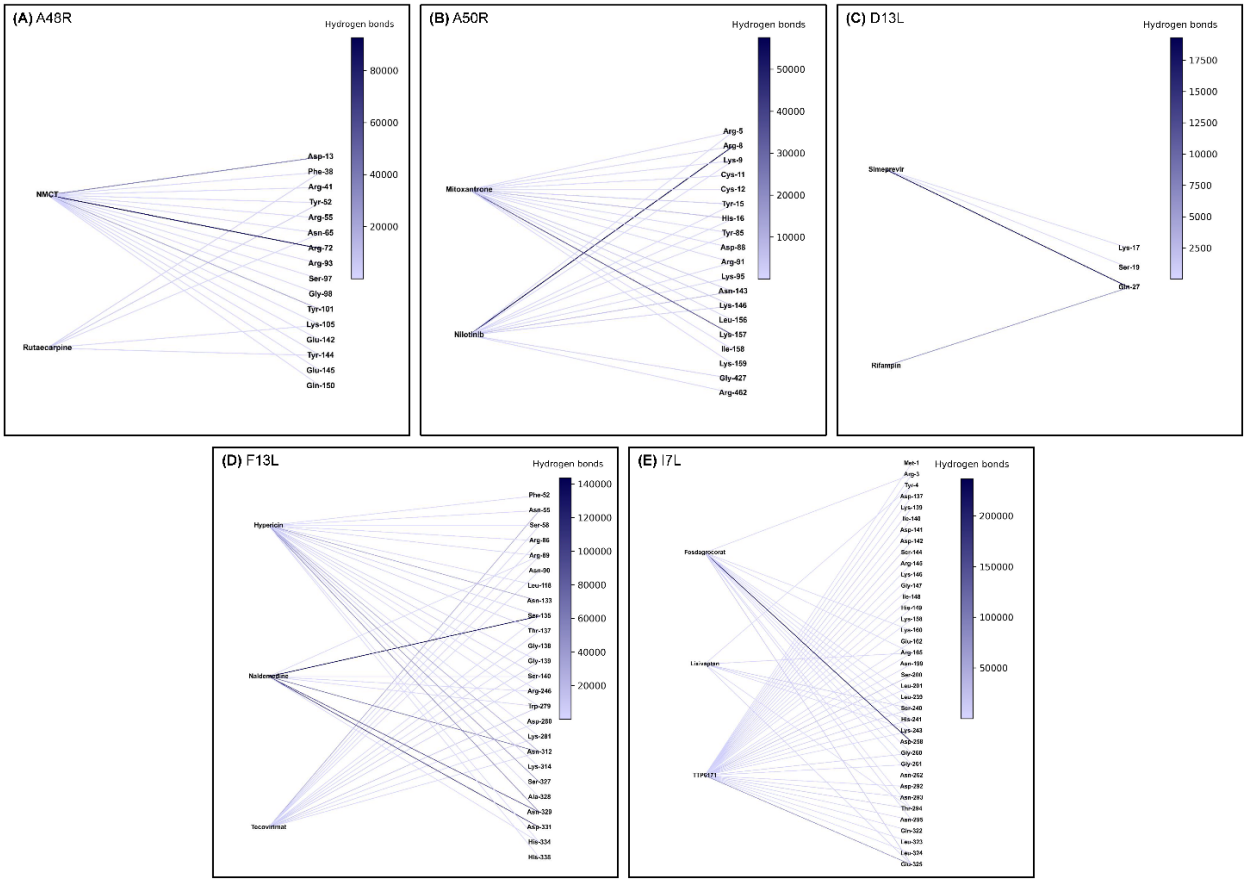

Figure 5. Hydrogen bonds to potential residues of interest. Hydrogen bonds were calculated with a cutoff of 0.3 nm and 30 degrees in GROMACS for the whole 100 ns simulation. Colour intensity indicates the number of hydrogen bonds to a specific residue summed throughout the simulation.

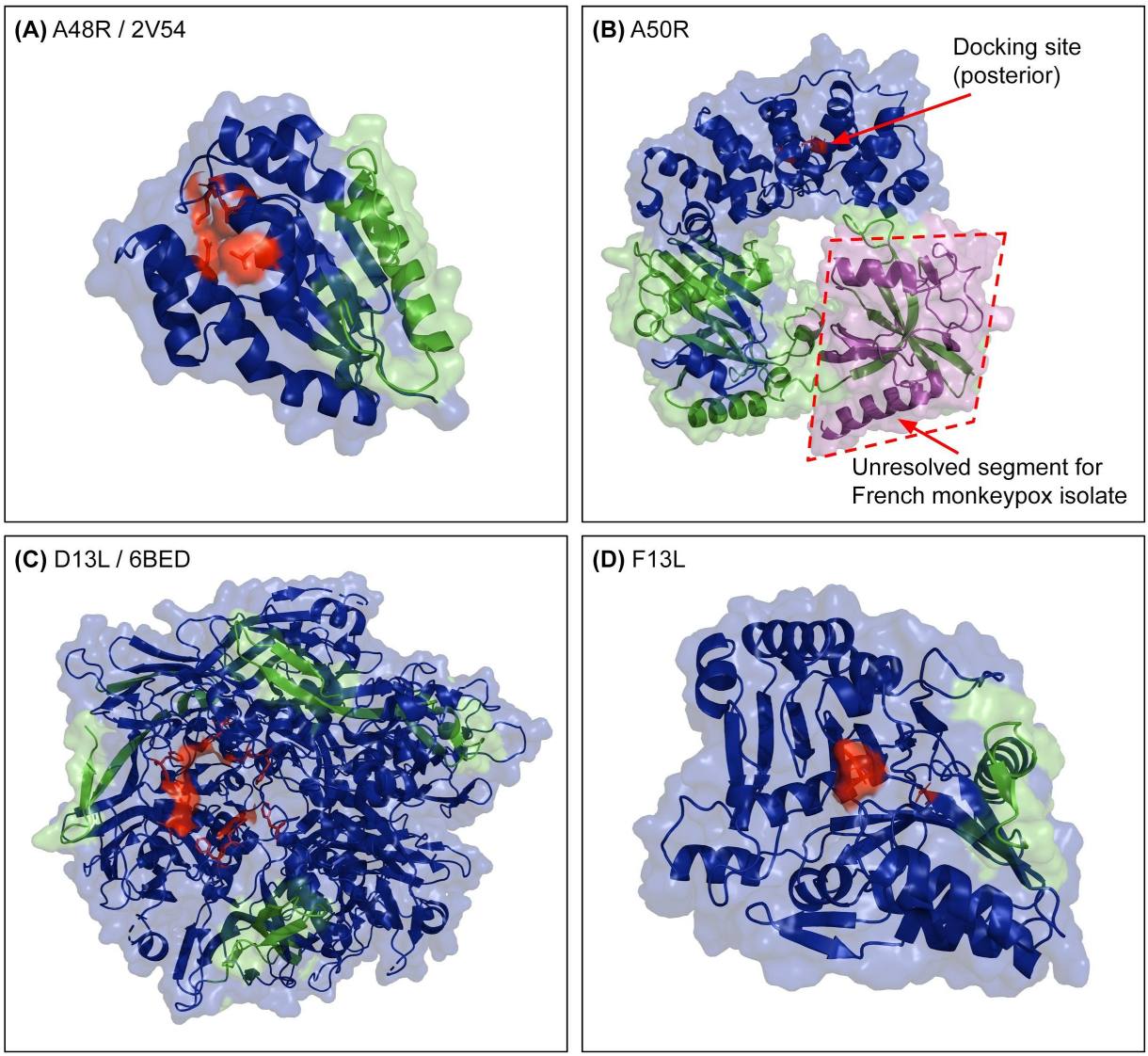

Supplementary figure 1. Sites of deletion are away from the active site for the French isolate. Active site is shown in red. Regions where premature stop codons were inserted and subsequent frames are shown in green, and the purple region in (b) A50R completely unresolved in the French isolate. The docking site of A50R is posterior relative to the view. Blue regions show high conservation throughout all isolates of monkeypox, smallpox and vaccinia investigated.

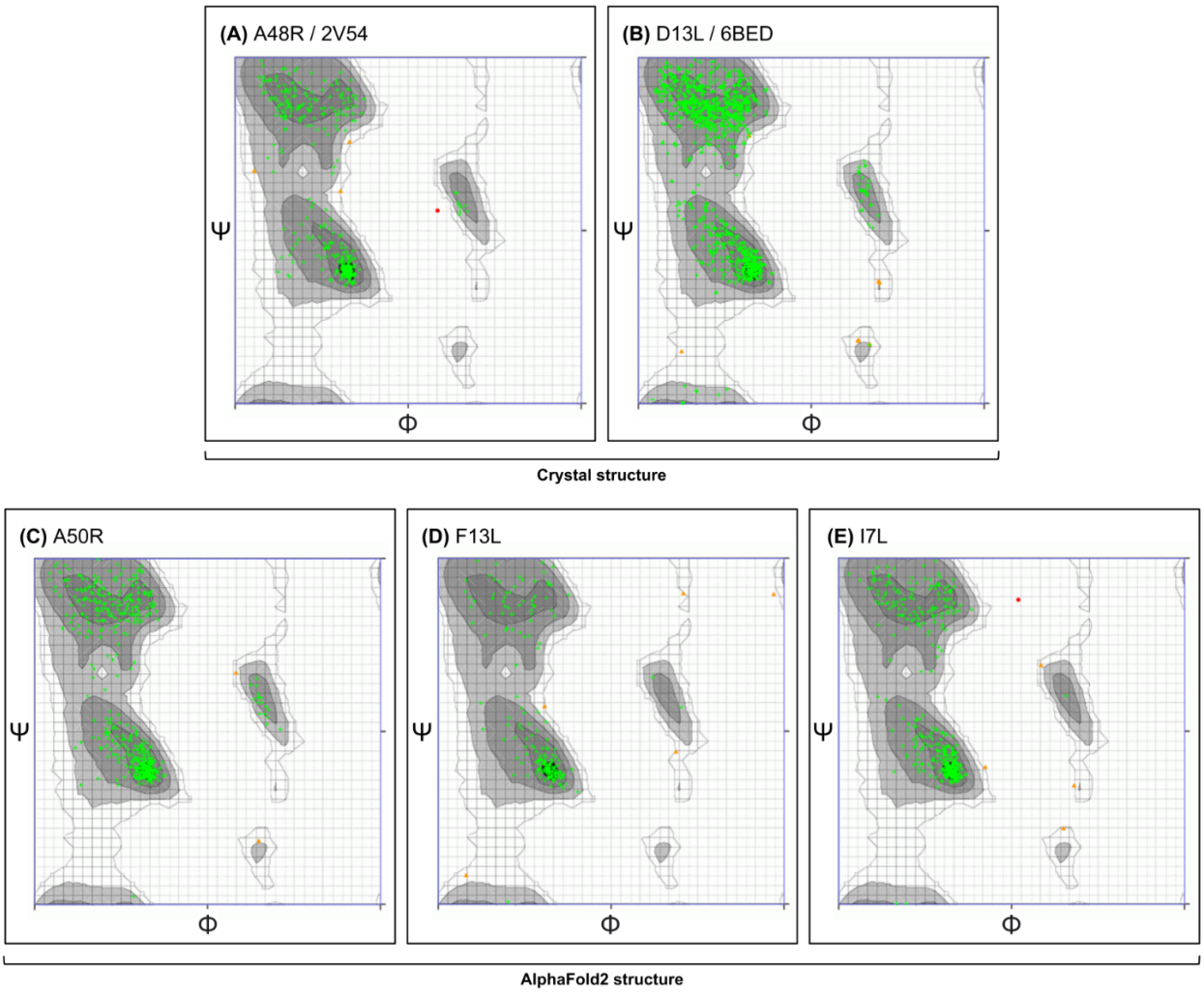

Supplementary figure 2. Overall stability in phi and psi bonds in proteins used for screening. (a, b) Structures determined using X-ray crystallography and (c, d, e) through AlphaFold2 were put into the Ramachandran server.

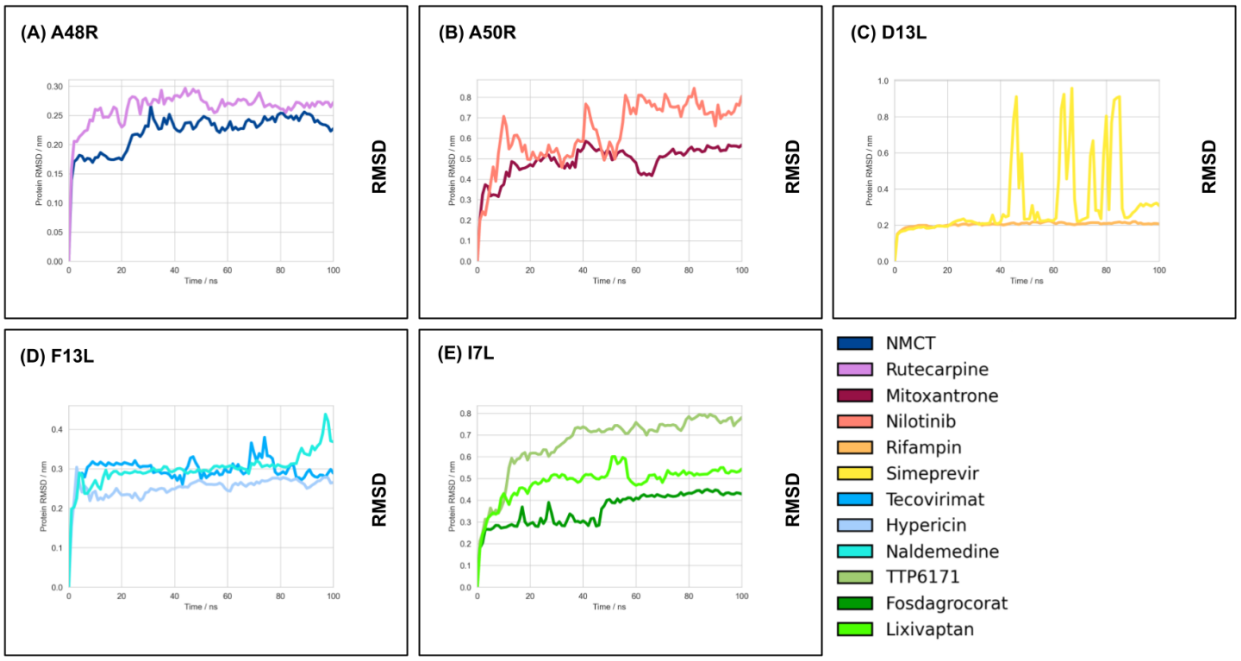

Supplementary figure 3. Overall stability of protein structures in MD simulations, with no drastic changes in protein structure. Proteins were centred, adjusted for PBC, and fitted to the pocket of interest and RMSD calculated relative to the initial structure using GROMACS.

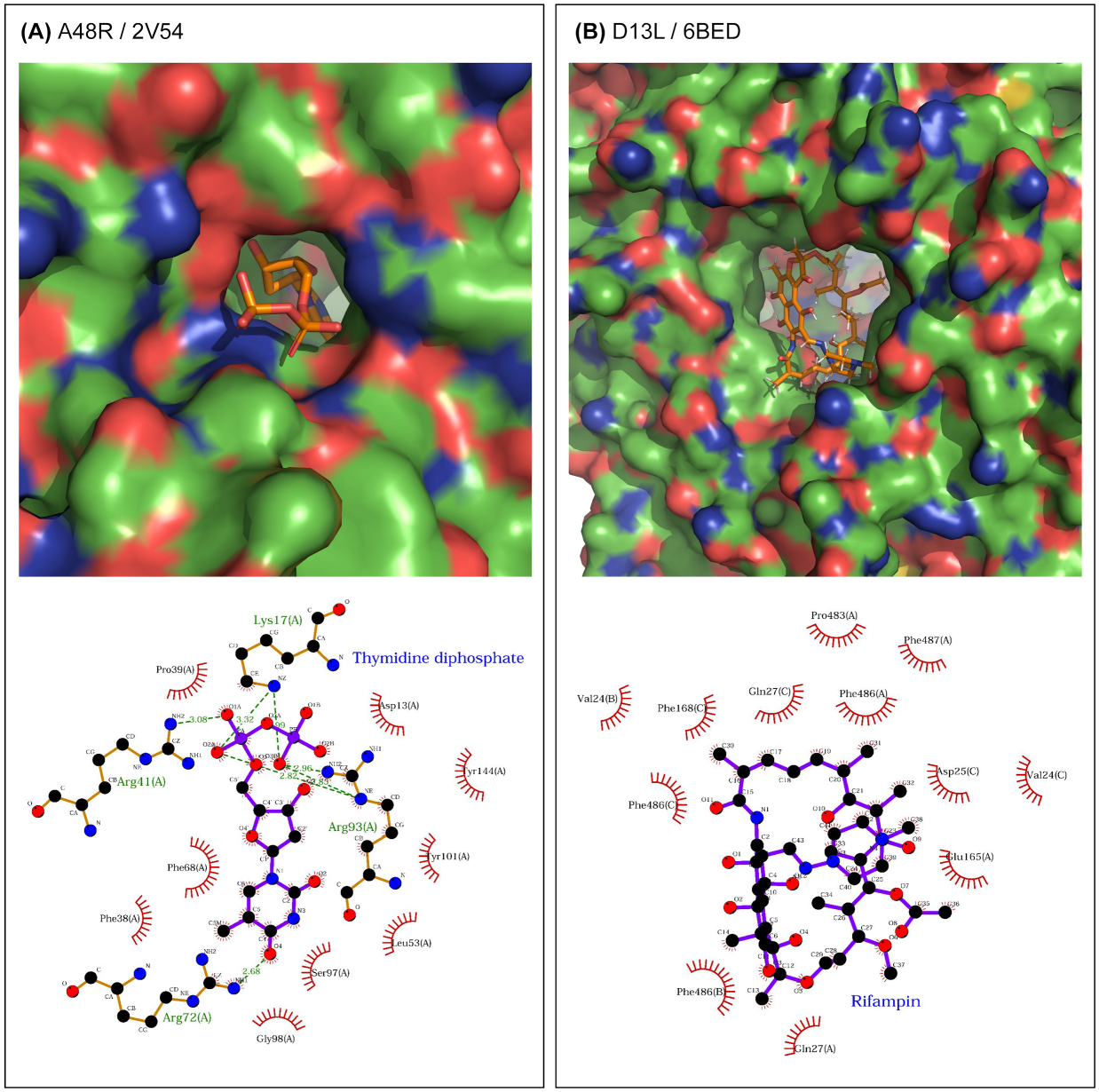

Supplementary figure 4. Original poses of X-ray elucidated structures and their respective non-bonded interactions. (a) A48R was referenced from 2V54, with a docked thymidine 5'-diphosphate molecule. (b) D13L was referenced from 6BED, with a docked rifampin molecule. Waters and other molecules were removed before analysis. LigPLOT+ was used to generate the ligand interaction figures.

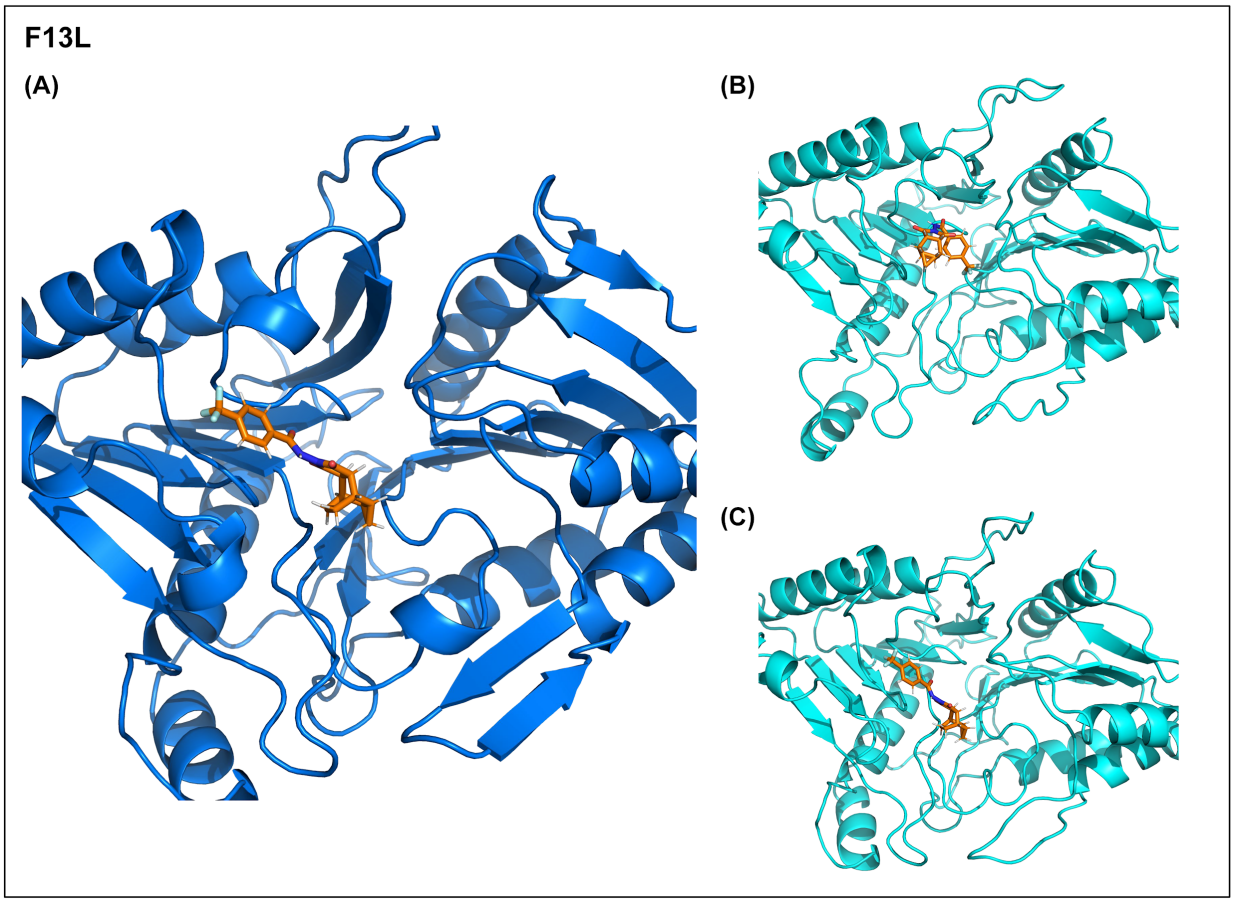

Supplementary figure 5. Most stable pose of tecovirimat in F13L is inverted as opposed to the original pose proposed by QVina2.1. (a) Most clustered pose was determined using GROMACS clustering with GROMOS force field at a cutoff value of RMSD 0.3 nm. (b) Structure of tecovirimat and protein at t = 0 ps of the simulation and structure of tecovirimat and protein at t = 100,000 ps of the simulation.

Supplementary file 1: binding energies per QVina2.1 score for all drugs screened.

Supplementary file 2: summarised PDB trajectories and RMSF values for protein residues. PDB trajectories were centred, adjusted for PBC, and fitted to the pocket of interest. Each frame is 2.5 ns. RMSF calculations were performed using GROMACS.

References

1. Macneil, A., et al., *Transmission of atypical varicella-zoster virus infections involving palm and sole manifestations in an area with monkeypox endemicity.* Clin Infect Dis, 2009. **48**(1): p. e6-8.
2. Bunge, E.M., et al., *The changing epidemiology of human monkeypox-A potential threat? A systematic review.* PLoS Negl Trop Dis, 2022. **16**(2): p. e0010141.
3. Yong, S.E.F., et al., *Imported Monkeypox, Singapore.* Emerg Infect Dis, 2020. **26**(8): p. 1826-1830.
4. Vaughan, A., et al., *Two cases of monkeypox imported to the United Kingdom, September 2018.* Euro Surveill, 2018. **23**(38).
5. Erez, N., et al., *Diagnosis of Imported Monkeypox, Israel, 2018.* Emerg Infect Dis, 2019. **25**(5): p. 980-983.
6. CDC, U.S., *U.S. Monkeypox Outbreak 2022: Situation Summary*, C.f.D.C.a. Prevention, Editor. 2022: cdc.com.
7. Ligon, B.L., *Monkeypox: a review of the history and emergence in the Western hemisphere.* Semin Pediatr Infect Dis, 2004. **15**(4): p. 280-7.
8. Vallee, A., E. Farfour, and D. Zucman, *Monkeypox virus: A novel sexually transmitted disease? A case report from France.* Travel Med Infect Dis, 2022. **49**: p. 102394.
9. Tesini, B.L. *Monkeypox*. 2020; Available from: https://www.msdmanuals.com/en-sg/professional/infectious-diseases/pox-viruses/monkeypox.
10. Damon, I.K., *Status of human monkeypox: clinical disease, epidemiology and research.* Vaccine, 2011. **29 Suppl 4**: p. D54-9.
11. Reynolds, M.G., et al., *Improving the Care and Treatment of Monkeypox Patients in Low-Resource Settings: Applying Evidence from Contemporary Biomedical and Smallpox Biodefense Research.* Viruses, 2017. **9**(12).
12. Shchelkunov, S.N., et al., *Human monkeypox and smallpox viruses: genomic comparison.* FEBS Lett, 2001. **509**(1): p. 66-70.
13. Senkevich, T.G., et al., *Ancient Gene Capture and Recent Gene Loss Shape the Evolution of Orthopoxvirus-Host Interaction Genes.* mBio, 2021. **12**(4): p. e0149521.
14. Jacobs, B.L., et al., *Vaccinia virus vaccines: past, present and future.* Antiviral Res, 2009. **84**(1): p. 1-13.
15. MacNeil, A., M.G. Reynolds, and I.K. Damon, *Risks associated with vaccinia virus in the laboratory.* Virology, 2009. **385**(1): p. 1-4.
16. Kugelman, J.R., et al., *Genomic variability of monkeypox virus among humans, Democratic Republic of the Congo.* Emerg Infect Dis, 2014. **20**(2): p. 232-9.
17. Massung, R.F., et al., *Analysis of the complete genome of smallpox variola major virus strain Bangladesh-1975.* Virology, 1994. **201**(2): p. 215-40.
18. Prazsak, I., et al., *Full Genome Sequence of the Western Reserve Strain of Vaccinia Virus Determined by Third-Generation Sequencing.* Genome Announc, 2018. **6**(11).
19. Prichard, M.N. and E.R. Kern, *Orthopoxvirus targets for the development of new antiviral agents.* Antiviral Res, 2012. **94**(2): p. 111-25.
20. Caillat, C., et al., *Crystal structure of poxvirus thymidylate kinase: an unexpected dimerization has implications for antiviral therapy.* Proc Natl Acad Sci U S A, 2008. **105**(44): p. 16900-5.
21. Deng, L., et al., *Identification of novel antipoxviral agents: mitoxantrone inhibits vaccinia*

virus replication by blocking virion assembly. J Virol, 2007. **81**(24): p. 13392-402.
22. Bahar, M.W., et al., *Insights into the evolution of a complex virus from the crystal structure of vaccinia virus D13.* Structure, 2011. **19**(7): p. 1011-20.
23. Beloor Suresh, A., A. Rosani, and R. Wadhwa, *Rifampin*, in *StatPearls*. 2022: Treasure Island (FL).
24. Garriga, D., et al., *Structural basis for the inhibition of poxvirus assembly by the antibiotic rifampicin.* Proc Natl Acad Sci U S A, 2018. **115**(33): p. 8424-8429.
25. Grimley, P.M., et al., *Interruption by Rifampin of an early stage in vaccinia virus morphogenesis: accumulation of membranes which are precursors of virus envelopes.* J Virol, 1970. **6**(4): p. 519-33.
26. Subak-Sharpe, J.H., M.C. Timbury, and J.F. Williams, *Rifampicin inhibits the growth of some mammalian viruses.* Nature, 1969. **222**(5191): p. 341-5.
27. Tan, K.B. and B.R. McAuslan, *Effect of rifampicin on poxvirus protein synthesis.* J Virol, 1970. **6**(3): p. 326-32.
28. Moss, B., et al., *Rifamycins: modulation of specific anti-poxviral activity by small substitutions on the piperazinyliminomethyl side chain.* Antimicrob Agents Chemother, 1972. **2**(3): p. 181-5.
29. Moss, B., *Membrane fusion during poxvirus entry.* Semin Cell Dev Biol, 2016. **60**: p. 89-96.
30. Jordan, R., et al., *Development of ST-246(R) for Treatment of Poxvirus Infections.* Viruses, 2010. **2**(11): p. 2409-35.
31. Byrd, C.M., et al., *New class of orthopoxvirus antiviral drugs that block viral maturation.* J Virol, 2004. **78**(22): p. 12147-56.
32. Zephyr, J., N. Kurt Yilmaz, and C.A. Schiffer, *Viral proteases: Structure, mechanism and inhibition.* Enzymes, 2021. **50**: p. 301-333.
33. Steuber, H. and R. Hilgenfeld, *Recent advances in targeting viral proteases for the discovery of novel antivirals.* Curr Top Med Chem, 2010. **10**(3): p. 323-45.
34. Gasteiger, E., et al., *ExPASy: The proteomics server for in-depth protein knowledge and analysis.* Nucleic Acids Res, 2003. **31**(13): p. 3784-8.
35. Corpet, F., *Multiple sequence alignment with hierarchical clustering.* Nucleic Acids Res, 1988. **16**(22): p. 10881-90.
36. Jumper, J., et al., *Highly accurate protein structure prediction with AlphaFold.* Nature, 2021. **596**(7873): p. 583-589.
37. Mirdita, M., et al., *ColabFold: making protein folding accessible to all.* Nat Methods, 2022. **19**(6): p. 679-682.
38. Yang, G., et al., *An orally bioavailable antipoxvirus compound (ST-246) inhibits extracellular virus formation and protects mice from lethal orthopoxvirus Challenge.* J Virol, 2005. **79**(20): p. 13139-49.
39. Alhossary, A., et al., *Fast, accurate, and reliable molecular docking with QuickVina 2.* Bioinformatics, 2015. **31**(13): p. 2214-6.
40. Irwin, J.J. and B.K. Shoichet, *ZINC--a free database of commercially available compounds for virtual screening.* J Chem Inf Model, 2005. **45**(1): p. 177-82.
41. Wishart, D.S., et al., *DrugBank 5.0: a major update to the DrugBank database for 2018.* Nucleic Acids Res, 2018. **46**(D1): p. D1074-D1082.
42. Law, V., et al., *DrugBank 4.0: shedding new light on drug metabolism.* Nucleic Acids Res, 2014. **42**(Database issue): p. D1091-7.
43. Ravindranath, P.A., et al., *AutoDockFR: Advances in Protein-Ligand Docking with Explicitly Specified Binding Site Flexibility.* PLoS Comput Biol, 2015. **11**(12): p.

e1004586.
44. DeLano, W.L., *PyMOL(TM) Molecular Graphics System*. 2022, Schrödinger, LLC.
45. O'Boyle, N.M., et al., *Open Babel: An open chemical toolbox.* J Cheminform, 2011. **3**: p. 33.
46. Pronk, S., et al., *GROMACS 4.5: a high-throughput and highly parallel open source molecular simulation toolkit.* Bioinformatics, 2013. **29**(7): p. 845-54.
47. Jo, S., et al., *CHARMM-GUI: a web-based graphical user interface for CHARMM.* J Comput Chem, 2008. **29**(11): p. 1859-65.
48. Lee, J., et al., *CHARMM-GUI Input Generator for NAMD, GROMACS, AMBER, OpenMM, and CHARMM/OpenMM Simulations Using the CHARMM36 Additive Force Field.* J Chem Theory Comput, 2016. **12**(1): p. 405-13.
49. Coutsias, E.A., et al., *A kinematic view of loop closure.* J Comput Chem, 2004. **25**(4): p. 510-28.
50. Anderson, R.J., et al., *Main-chain conformational tendencies of amino acids.* Proteins, 2005. **60**(4): p. 679-89.
51. Christen, M., et al., *The GROMOS software for biomolecular simulation: GROMOS05.* J Comput Chem, 2005. **26**(16): p. 1719-51.
52. Laskowski, R.A. and M.B. Swindells, *LigPlot+: multiple ligand-protein interaction diagrams for drug discovery.* J Chem Inf Model, 2011. **51**(10): p. 2778-86.
53. Kern, E.R., et al., *Activities of certain 5-substituted 4'-thiopyrimidine nucleosides against orthopoxvirus infections.* Antimicrob Agents Chemother, 2009. **53**(2): p. 572-9.
54. Marquez, V.E., et al., *The history of N-methanocarbathymidine: the investigation of a conformational concept leads to the discovery of a potent and selective nucleoside antiviral agent.* Antiviral Res, 2006. **71**(2-3): p. 268-75.
55. Tian, K.M., J.J. Li, and S.W. Xu, *Rutaecarpine: A promising cardiovascular protective alkaloid from Evodia rutaecarpa (Wu Zhu Yu).* Pharmacol Res, 2019. **141**: p. 541-550.
56. Staffeldt, B., et al., *Pharmacokinetics of hypericin and pseudohypericin after oral intake of the hypericum perforatum extract LI 160 in healthy volunteers.* J Geriatr Psychiatry Neurol, 1994. **7 Suppl 1**: p. S47-53.
57. Bowman, B.T. and M.H. Rosner, *Lixivaptan - an evidence-based review of its clinical potential in the treatment of hyponatremia.* Core Evid, 2013. **8**: p. 47-56.
58. Charity, J.C., E. Katz, and B. Moss, *Amino acid substitutions at multiple sites within the vaccinia virus D13 scaffold protein confer resistance to rifampicin.* Virology, 2007. **359**(1): p. 227-32.
59. Quenelle, D.C., et al., *Efficacy of orally administered low dose N-methanocarbathymidine against lethal herpes simplex virus type-2 infections of mice.* Antivir Chem Chemother, 2011. **22**(3): p. 131-7.
60. Zalah, L., et al., *Metabolic pathways of N-methanocarbathymidine, a novel antiviral agent, in native and herpes simplex virus type 1 infected Vero cells.* Antiviral Res, 2002. **55**(1): p. 63-75.
61. Jayakumar, T., et al., *Anti-Inflammatory Mechanism of An Alkaloid Rutaecarpine in LTA-Stimulated RAW 264.7 Cells: Pivotal Role on NF-kappaB and ERK/p38 Signaling Molecules.* Int J Mol Sci, 2022. **23**(11).
62. Izquierdo, L., et al., *Simeprevir for the treatment of hepatitis C virus infection.* Pharmgenomics Pers Med, 2014. **7**: p. 241-9.
63. Collins, J.M., et al., *Hepatitis B Virus Reactivation During Successful Treatment of Hepatitis C Virus With Sofosbuvir and Simeprevir.* Clin Infect Dis, 2015. **61**(8): p. 1304-6.
64. Kubin, A., et al., *Hypericin--the facts about a controversial agent.* Curr Pharm Des, 2005.

11(2): p. 233-53.
65. Jendzelovska, Z., et al., *Hypericin in the Light and in the Dark: Two Sides of the Same Coin.* Front Plant Sci, 2016. **7**: p. 560.
66. Delcanale, P., et al., *The Interaction of Hypericin with SARS-CoV-2 Reveals a Multimodal Antiviral Activity.* ACS Appl Mater Interfaces, 2022. **14**(12): p. 14025-14032.
67. Hudson, J.B., I. Lopez-Bazzocchi, and G.H. Towers, *Antiviral activities of hypericin.* Antiviral Res, 1991. **15**(2): p. 101-12.
68. Nicolussi, S., et al., *Clinical relevance of St. John's wort drug interactions revisited.* Br J Pharmacol, 2020. **177**(6): p. 1212-1226.
69. Murphy, P.A., et al., *Interaction of St. John's Wort with oral contraceptives: effects on the pharmacokinetics of norethindrone and ethinyl estradiol, ovarian activity and breakthrough bleeding.* Contraception, 2005. **71**(6): p. 402-8.
70. Kalb, R., R.D. Trautmann-Sponsel, and M. Kieser, *Efficacy and tolerability of hypericum extract WS 5572 versus placebo in mildly to moderately depressed patients. A randomized double-blind multicenter clinical trial.* Pharmacopsychiatry, 2001. **34**(3): p. 96-103.
71. Kanemasa, T., et al., *Pharmacologic effects of naldemedine, a peripherally acting mu-opioid receptor antagonist, in in vitro and in vivo models of opioid-induced constipation.* Neurogastroenterol Motil, 2019. **31**(5): p. e13563.
72. Blair, H.A., *Naldemedine: A Review in Opioid-Induced Constipation.* Drugs, 2019. **79**(11): p. 1241-1247.
73. Katakami, N., et al., *Randomized Phase III and Extension Studies of Naldemedine in Patients With Opioid-Induced Constipation and Cancer.* J Clin Oncol, 2017. **35**(34): p. 3859-3866.
74. Weatherley, B., L. McFadyen, and B. Tammara, *Population Pharmacokinetics of Fosdagrocorat (PF-04171327), a Dissociated Glucocorticoid Receptor Agonist, in Patients With Rheumatoid Arthritis.* Clin Transl Sci, 2018. **11**(1): p. 54-62.
75. Di Mise, A., et al., *Lixivaptan, a New Generation Diuretic, Counteracts Vasopressin-Induced Aquaporin-2 Trafficking and Function in Renal Collecting Duct Cells.* Int J Mol Sci, 2019. **21**(1).
76. White, J.M., et al., *Drug Combinations as a First Line of Defense against Coronaviruses and Other Emerging Viruses.* mBio, 2021. **12**(6): p. e0334721.